JACS
JOURNAL OF THE AMERICAN CHEMICAL SOCIETY

ARTICLE

pubs.acs.org/JACS

Reaction Pathways of Proton Transfer in Hydrogen-Bonded Phenol−Carboxylate Complexes Explored by Combined UV−Vis and NMR Spectroscopy

Benjamin Koeppe,[†] Peter M. Tolstoy,[*,†,‡,§] and Hans-Heinrich Limbach[†]

[†]Institut für Chemie und Biochemie, Freie Universität Berlin, Takustrasse 3, D-14195 Berlin, Germany

[‡]V.A. Fock Institute of Physics, St. Petersburg State University, Uljanovskaja 1, 198504 St. Petersburg, Russia

Supporting Information

ABSTRACT: Combined low-temperature NMR/UV−vis spectroscopy (UVNMR), where optical and NMR spectra are measured in the NMR spectrometer under the same conditions, has been set up and applied to the study of H-bonded anions A··H··X$^-$ (AH = 1-^{13}C-2-chloro-4-nitrophenol, X$^-$ = 15 carboxylic acid anions, 5 phenolates, Cl$^-$, Br$^-$, I$^-$, and BF_4^-). In this series, H is shifted from A to X, modeling the proton-transfer pathway. The ^{1}H and ^{13}C chemical shifts and the H/D isotope effects on the latter provide information about averaged H-bond geometries. At the same time, red shifts of the $\pi-\pi^*$ UV−vis absorption bands are observed which correlate with the averaged H-bond geometries. However, on the UV−vis time scale, different tautomeric states and solvent configurations are in slow exchange. The combined data sets indicate that the proton transfer starts with a H-bond compression and a displacement of the proton toward the H-bond center, involving single-well configurations A−H···X$^-$. In the strong H-bond regime, coexisting tautomers A··H···X$^-$ and A$^-$···H··X are observed by UV. Their geometries and statistical weights change continuously when the basicity of X$^-$ is increased. Finally, again a series of single-well structures of the type A$^-$···H−X is observed. Interestingly, the UV−vis absorption bands are broadened inhomogeneously because of a distribution of H-bond geometries arising from different solvent configurations.

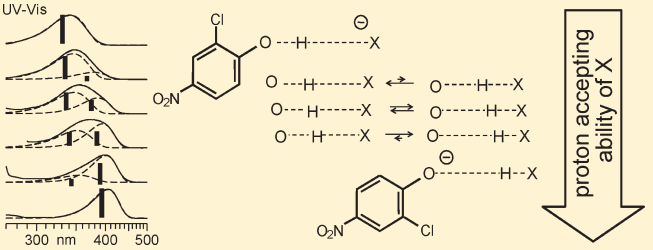

INTRODUCTION

Hydrogen-bond-mediated intermolecular acid−base interactions are of prime importance for the function of biomolecules.[1,2] They depend strongly on the environment. In aqueous solution, acid−base interactions are characterized by pK_a values, which allow one to calculate the equilibrium constant of proton transfer between the solvated acid and the solvated base. However, this concept breaks down when AH and B form a direct hydrogen bond, AHB, for example in environments such as the organic solid state, aprotic solvents, or the interior of proteins. The location of H may depend not only on the acidity of AH and the basicity of B but also on the local electrostatics. The pathways of proton transfer between A and B have been explored by neutron crystallography[3] and solid-state NMR[4] of series of hydrogen-bonded complexes, where each complex is assumed to represent a snapshot of the proton-transfer pathway. These studies showed that when the acidity of AH is increased, H transfer to B occurs via a series of geometric states, A··H·····B via A··H··B to A·····H··B, where a compression of the intermolecular hydrogen bond occurs when H is shifted toward the H-bond center. Similar effects were observed for isolated complexes in the gas phase exposed to strong electric fields.[5] Solid- and liquid-state NMR H-bond correlations indicated typical changes of NMR parameters during this process.[6−8] The most important change is the chemical shift of the hydrogen-bonded proton, which senses the H-bond compression by a low-field shift,[9−11] whereas signals of heavy atoms such as ^{15}N and ^{19}F probe the proton position,[12,13] as well as H/D isotope effects on chemical shifts.[10,14−16] In cases of hydrogen bonds formed by carboxylic acids, the NMR parameters of carboxylic carbon atoms have been exploited.[10,15−17]

These NMR correlations have been applied to liquid solutions in order to establish averaged H-bond geometries.[18] However, the proton-transfer pathway of Figure 1a, corresponding to a sequence of averaged H-bond geometries, constitutes a crude model which does not explicitly take into account the possibility of single- or double-well potentials, nor distributions of H-bond geometries arising from solute−solvent interactions.[19] The latter have also been called "solvatomers".[20]

Using the NMR method of isotopic perturbation, Perrin et al. obtained evidence in the case of several intramolecular hydrogen-bonded systems for the absence of quasi-symmetric structures A··H··B and the presence of tautomeric equilibria, as illustrated in Figure 1b, characterized by an equilibrium constant K.[21] An increase of the acidity of AH then leads to an increase of

Received: February 4, 2011
Published: May 02, 2011

dx.doi.org/10.1021/ja201113a | J. Am. Chem. Soc. 2011, 133, 7897–7908

K and hence to H transfer from A to B. However, it has not yet been possible to determine the geometries of the tautomers or to solve the question of how far the protons are transferred, whether the jump distances are smaller than proton displacements caused by the solvent cages as has been discussed previously,[20] and hence whether tautomers are clearly separated from solvatomers.

In contrast to NMR, which is not able to follow H transfers in strong hydrogen bonds in solution in real time, optical spectroscopy is able to distinguish an acid and its deprotonated base. Thus, using UV−vis spectroscopy, tautomeric equilibria have been previously detected for complexes of phenols with proton acceptors.[22−26] Unfortunately, the spectra of solutions of AH and B are often influenced by a number of different hydrogen-bonded species such as homoconjugated complexes AHA^- and BHB^+, as well as higher associates of the type $(AH)_nB_m$, which makes the analysis often difficult. Moreover, potential information about H-bond geometries from UV−vis spectra has not been exploited to our knowledge, so again it is difficult to obtain information about the potential energy surface of the proton motion by UV−vis spectroscopy.

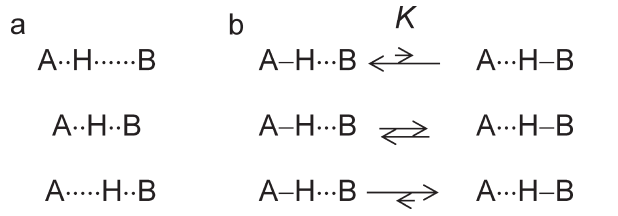

Figure 1. H-transfer pathways from an acid A to a base B in a hydrogen bond AHB upon an increase of the acidity of AH. (a) Continuous change of the H-bond geometry from the initial to the final state, assisted by H-bond compression when H approaches the H-bond center. (b) Traditional proton-transfer equilibrium between A and B.

However, if links between UV−vis bands and H-bond geometries could be established, this not only would be of importance for understanding the pathways of proton transfer in solution but also may have important applications in biophysics. For example, photoactive proteins such as the photoactive yellow protein (PYP) contain a phenolic cofactor hydrogen-bonded to a carboxylate,[27] which after photoexcitation forms a series of structural intermediates exhibiting characteristic absorption frequencies.[28] However, the associated changes in the H-bond geometries are largely unknown to date.

In order to establish the desired correlation between H-bond geometries and UV−vis parameters, we have proposed the use of combined low-temperature UV−vis and NMR spectroscopy (UVNMR), where both types of spectra are measured at the same time for a single sample under the same conditions. The setup for this technique has been described recently.[29] The NMR spectrum allows one to determine the structure of the complexes present in the sample, i.e., removes the existing uncertainties of UV−vis spectroscopy, and allows one to obtain information about the averaged H-bond geometries from NMR chemical shifts. Thus, the high potential of UV−vis spectroscopy to detect fast dynamics, averaged out in NMR spectra, can be exploited, and UV−vis bands can be correlated with H-bond geometries.

To model interactions in photoactive proteins, we have chosen to perform low-temperature UVNMR studies of anionic AHX^- hydrogen-bonded complexes depicted in Figure 2, where AH = 2-chloro-4-nitrophenol (**1**) and X^- = 2-chloro-4-nitrophenolate **2** (A^-), 15 carboxylate anions, 6 phenolates, and the halogen anions Cl^-, Br^-, I^-, and BF_4^-. In addition, we have studied the neutral AH (**1**) and its anion A^- (**2**) (see Figure 2).

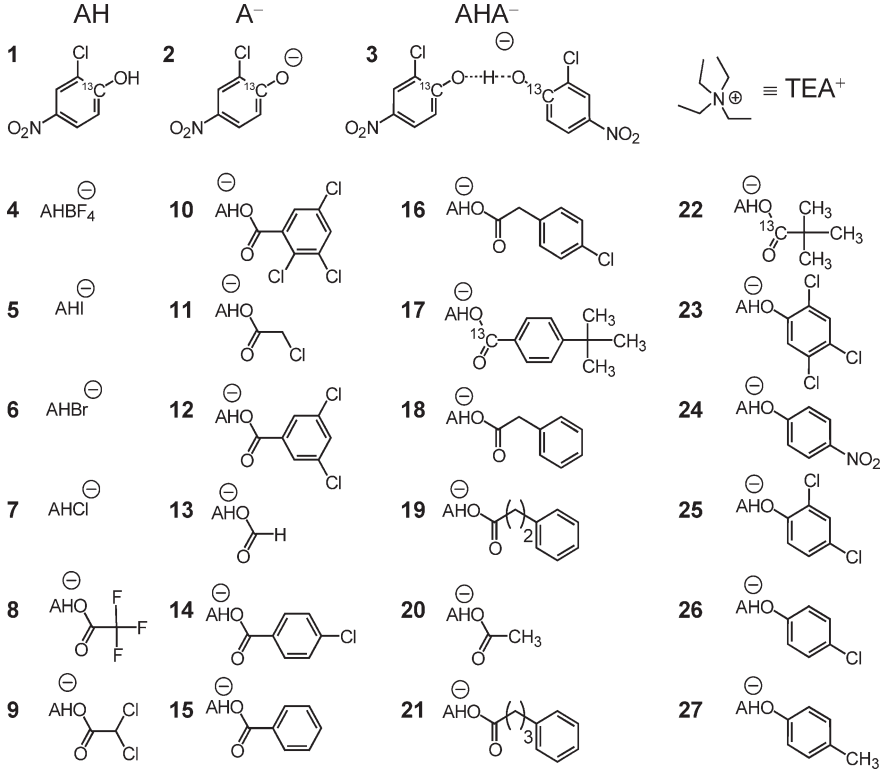

Figure 2. Structures of studied species: 2-chloro-4-nitrophenol (**1**), its anion **2**, and its hydrogen-bonded conjugated complexes with the given acids and phenols, **3**−**27**. Positions of bridging protons in complexes vary as discussed in the text.

dx.doi.org/10.1021/ja201113a |*J. Am. Chem. Soc.* 2011, 133, 7897–7908

In all cases, tetraethylammonium (TEA) was used as a countercation. As solvent we used CD_2Cl_2 down to its freezing point at −97 °C. We chose **1** as chromophore because it is a rather acidic phenol and can mimic the acidity increase of weaker acids upon photoexcitation, allowing one to detect a wide range of protonation states in complexes with anions of carboxylic acids and other phenols. In this paper we will refer to the 2-chloro-4-nitrophenolate moiety as the "chromophore" in all of its forms, be it neutral AH, anionic A^-, or part of an AHX^- complex.

This paper is structured as follows. After the Experimental Section, the results of our UVNMR measurements are presented and discussed. A correlation between UV-band frequencies and H-bond geometries is proposed, and the range of geometries is specified in which a tautomeric equilibrium is present. Based thereupon, a qualitative description of the proton-transfer pathway is presented which may, in the future, be extended to a quantitative description.

EXPERIMENTAL SECTION

Synthesis of 1-^{13}C-2-Chloro-4-nitrophenol (1). 1-^{13}C-4-Nitrophenol was obtained by cyclization[30] of 2-^{13}C-acetone with sodium nitromalonaldehyde.[31] The latter was then converted into 1-^{13}C-2-chloro-4-nitrophenol (**1**) using a well-established procedure[32] which had, however, to be adapted to a small scale as described in the following. First, 0.10 g of 1-^{13}C-4-nitrophenol was dissolved in 10 mL of 25% aqueous HCl with gentle heating. The solution was cooled in an ice bath under vigorous stirring, upon which it formed a gel. Under continued stirring, 0.35 mL of sodium hypochlorite solution (150 g/L) was added dropwise within 2 min. After 1 h of continued stirring, the reaction mixture was extracted with diethyl ether. The organic phase was separated and dried. The solvent was evaporated, yielding 0.11 g of the crude product. Removal of a yellow impurity was achieved by preparative thin-layer chromatography (TLC, silica; dichloromethane/methanol 20:1). Residual starting material, if present, was removed by recrystallization from 25% aqueous HCl.

General Techniques for the Preparation of UVNMR and NMR Samples. To facilitate the sample preparation, certain preliminary and general actions were taken, which are described below. The specific details for each of the samples are given in the following subsections.

Stock Solutions. Stock solutions, 5−100 mM (0.5 mL), of the different acids and phenols in dry CD_2Cl_2, CH_2Cl_2, or methanol were prepared. For that purpose, substances were weighted and dissolved in 2 mL glass vials with PTFE lined screw caps (Wheaton). Solvents and solutions were handled with microliter pipets (Eppendorf). Mixing of the components for the sample preparation was based on these stock solutions.

Preparation of Tetraethylammonium Salts of Proton Donors HX. A certain amount (∼1−20 μmol) of HX (as stock solution) was mixed in a 10 mL flask with 0.7−1.0 equiv of TEA hydroxide in methanol solution. The solvents were removed on a rotary evaporator (40 °C water bath, <10 mbar). After pressure equilibration with inert gas, ∼1 mL of CH_2Cl_2 (dried over 4 Å molecular sieves) was added and evaporated in vacuum to remove residual methanol and water. The latter procedure was repeated twice, leaving the dry salt.

Deuteration of NMR Samples in Mobile Proton Sites. Whenever deuteration of the sample was needed, the NMR tube equipped with a J. Young valve and containing the already prepared sample (see below) was attached to a high-vacuum line, and the solvent was evaporated. About 0.2 mL of methanol-OD (99.5%) was added to the sample and subsequently evaporated. In samples with volatile components, a trade-off between the desirable complete evaporation of methanol and the danger of too high losses of sample substance needs to be considered. Finally, the sample is redissolved in CD_2Cl_2.

Specific Techniques for the Preparation of UV−Vis and NMR Samples. To obtain all the data on the species HA, A^-, and AHX^- described in this work, two types of experiments on two independent sample types were performed for each species. On the one sample (type A), combined low-temperature ^{1}H NMR and UV−vis (UVNMR) measurements were performed at concentrations of the chromophore moiety A^- of ∼1 mM. These kinds of samples were prepared in UVNMR cuvettes as described below. The other sample type (type B) served for ^{13}C NMR measurements and contained ∼3 mM 1-^{13}C-enriched A^- (and the corresponding amounts of other components) to increase the signal-to-noise ratios in ^{13}C NMR spectra. Samples of type B were prepared in NMR tubes of medium wall size equipped with J. Young valves (Norell). For each sample of each species and type of experiment, relative sample compositions determined by ^{1}H NMR are listed in the Supporting Information (SI) Table S1 and presented graphically in Figure S1. Procedural details will follow immediately. To ensure consistent the results, low-temperature ^{1}H NMR spectra of the samples of types A and B were compared, and it was verified that the ^{1}H peak positions were the same (0.06 ppm mean square deviation; see Figure S9). In other words, the 3-fold difference in the absolute concentration of the samples of types A and B did not affect the NMR results, apart from the improved sensitivity in the case of type B samples. In all samples, CD_2Cl_2 (99.9% or 99.7%, Eurisotop; 99.8%, Deutero, Armar) dried over 4 Å molecular sieves was used as the solvent; the overall sample volumes varied between 300 and 450 μL.

*Samples of 2-Chloro-4-nitrophenol (**1**).* A 1 mM solution of **1** and a 3 mM solution of 1-^{13}C-enriched **1** were used for UVNMR (typeA) and ^{13}C NMR (type B), respectively.

*Samples of TEA 2-Chloro-4-nitrophenolate (**2**).* For UVNMR (type A), 20 μmol of TEA pivalate (prepared from the acid as described above) acting as proton scavenger were dissolved in 300 μL of CD_2Cl_2 and transferred to a UVNMR cuvette. Next, 0.3 μmol of **1** as a 10 mM solution was added. For ^{13}C NMR (type B), 1 μmol of **2** was prepared from 1-^{13}C enriched **1** and TEA hydroxide as described in the previous subsection, dissolved in 350 μL of solvent, and transferred to a sample tube.

*Samples for Complexes **4**−**7**.* The appropriate commercially available salt TEA^+X^- was dried by repeated addition and evaporation of dry CH_2Cl_2 in a rotary evaporator, taken up in 350 μL of dry CD_2Cl_2, and transferred to a sample tube. To this were added ∼0.4 μmol of HA for UVNMR samples (type A) and ∼1.2 μmol HA for ^{13}C NMR samples (type B), readily yielding complexes **4**−**7** as the exclusive species containing chromophore moiety formed in CD_2Cl_2 solution at low temperature. Type B samples were deuterated in the mobile proton sites as described in the general procedure above.

*Samples for Complexes **8**−**27**.* The appropriate salt TEA^+X^- (freshly prepared as described above) was dissolved in 350 μL of dry CD_2Cl_2 and transferred to a sample tube. To this were added ∼0.4 μmol of HA for UVNMR samples (type A) and ∼1.2 μmol of HA for ^{13}C NMR samples (type B). A solution of the acid HA was then added stepwise under ^{1}H NMR monitoring in order to shift equilibria in the direction of the desired heteroconjugated complexes AHX^-. For type A (UVNMR) samples, the composition was carefully adjusted such that AHX^- became in good approximation the exclusive species containing the chromophore moiety at measurement conditions. This procedure is described in more detail in ref 29. In complexes **26** and **27**, exclusiveness in the optical spectra could not be obtained due to a rapid irradiation-induced blue-drift of absorption during measurement;[33] spectra of AHX^- complexes **26** and **27** were determined by measurements in the presence of chromophore anion A^- (**2**) and subsequent deconvolution. The UV−vis spectrum of **24** cannot be obtained easily under the given regime due to overlaps in absorption of the 2-chloro-4-nitrophenol

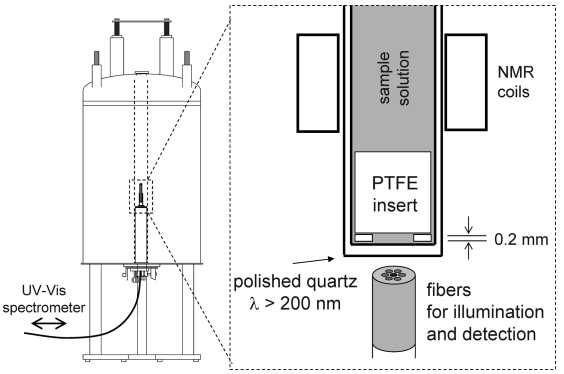

Figure 3. Experimental setup used for UVNMR experiments.

and 4-nitrophenol moieties. In all cases, type B samples were deuterated at the mobile proton sites, as described above (except for the sample of complex **20**, in which case acetic acid was found to be too volatile for the given procedure), as soon as a satisfactory fraction of AHX^- (ADX^-) was found. As a result, in type B sample, the AHX^- complex is not the exclusive form of the chromophore moiety.

Note that sample solutions of complexes, especially those containing weak proton donors, decompose on storage and irradiation due to nucleophilic attack of phenolates on dichloromethane;[33] various small amounts of coupling products were found in corresponding samples.

*Samples of Hydrogen Di-2-chloro-4-nitrophenolate (**3**).* A titration approach analogous to that used for the samples of heteroconjugated complexes **8**−**27** was employed. Sample solutions of appropriate amounts of 2-chloro-4-nitrophenolate (**2**) obtained from **1** and TEA hydroxide were prepared as described above, followed by a stepwise optimization by addition of a solution of **1**.

Acquisition and Processing of Combined ^{1}H NMR/UV−Vis and ^{13}C NMR Spectra. *UVNMR Measurements.* The experimental setup for a Bruker 500 MHz spectrometer shown in Figure 3 was similar to that described in ref 29, except for the following improvements. Samples were measured in "NMR cuvettes" custom-made by Hellma (Müllheim, Germany): the round bottoms of 5 mm quartz NMR sample tubes (0.8 mm wall size) were cut off and replaced by flat, optically polished quartz disks (0.4 mm thick). Inside the NMR cuvettes were placed PTFE inserts with 0.2 mm spacers, providing a homogeneous 0.4 mm optical path length for absorption measurements in reflection. Technical drawings of an NMR cuvette and a PTFE insert are given in SI Figure S2. Sample insertion depth in the NMR spinner was chosen such that samples rested on the optical reflection probe during measurements. Blank UV−vis measurements were performed prior to the actual sample measurements for each combination of NMR cuvette and PTFE insert using 50 μL of CD_2Cl_2 solvent at 200 K. ^{1}H NMR spectra were calibrated to $CHDCl_2$ (5.32 ppm). In all figures, UV−vis spectra were normalized to equal maxima in absorbance.

^{13}C NMR Measurements. For ^{13}C NMR measurements, a standard (not inversed) ^{1}H/^{13}C NMR probe was used. ^{13}C NMR spectra were calibrated to $^{13}CD_2Cl_2$ (53.5 ppm).

UV−Vis Spectra Deconvolution. For reasons that will become apparent in the Results and Discussion sections, UV−vis spectra were analyzed by least-squares fitting using log-normal band shapes in the wavenumber dimension.[34] For convenience, following the nomenclature of ref 34, the fitting function I was written as

$$I(\tilde{\nu}, A, \tilde{\nu}_0, H, \rho) = \frac{Ab}{\tilde{\nu} - b}\exp(-c^2)\exp\left(-\frac{1}{c^2}\left\{\ln\left(\frac{\tilde{\nu} - a}{b}\right)\right\}^2\right) \quad (1)$$

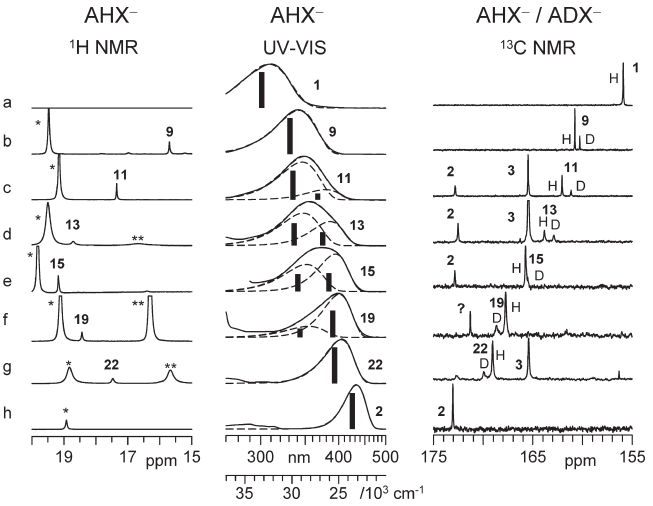

Figure 4. Partial experimental ^{1}H and ^{13}C NMR spectra and superimposed experimental and calculated UV−vis spectra of mixtures of 2-chloro-4-nitrophenol (**1**) with TEA carboxylates in CD_2Cl_2 around 175 K. The numbers on the peaks correspond to the species depicted in Figure 2. The dashed bands in the center column were calculated as described in the text.

where $a = \tilde{\nu}_0 - H\{\rho/(\rho^2 - 1)\}$, $b = H\{\rho/(\rho^2 - 1)\}\exp c^2$, and $c = \rho/(2\ln 2)^{1/2}$. The meanings of the four fitting parameters are as follows: A is the amplitude factor, $\tilde{\nu}_0$ is the wavenumber at the band's maximum, H is the full width at half-height, and ρ is the skewness.

For **1**, **2**, and complexes **4**−**9**, **22**−**27**, simply fitting with a single log-normal function gave good results (see Figure 4 and SI Figures S5 and S6). For all single log-normal fits, a skewness parameter of 1.5 was found to be satisfactory. For complexes **3**, **10**−**21**, the bands in the UV−vis spectra were fitted assuming the presence of two bands with asymmetry parameter of 1.5 and a bandwidth chosen as described in the Results section. The physical meaning of the bands and their widths will be addressed in the Discussion section. From the ^{1}H NMR spectra, we estimate that if there are other H-bonded complexes in solution which include **1** or **2** as one of the partners, the amount of such species does not exceed 5% of the main 1:1 complex. We estimate that this converts into the possible 5% error in the intensity of the fitted bands and in the error of the band position of no more than 5 nm.

Nomenclature. Throughout the paper, the chemical shifts of complexes **3**−**27** are labeled as δ(COHX), in which CO refers to the 1-C of **1** or **2** and its phenolic oxygen atom, and X to the acceptor atom in the partner (mostly oxygen). The observed nucleus is underlined. It should be clear from the context to which complex the chemical shift refers. For compounds **1** and **2**, the chemical shifts are denoted as δ(COH) and $\delta(CO^-)$, correspondingly. The H/D isotope effects on the chemical shift of the 1-C carbon of the 2-chloro-4-nitrophenyl moiety are defined as $\delta(\underline{C}ODX) - \delta(\underline{C}OHX)$.

RESULTS

UVNMR Spectroscopy. Selected spectral results obtained in this study for samples containing 1:1 complexes of 2-chloro-4-nitrophenolate (**2**) with carboxylic acids (HX) in CD_2Cl_2 are depicted in Figure 4. The signals are labeled by bold numbers which correspond to the structures of heteroconjugated complexes AHX^- and the homoconjugated complex AHA^- depicted in Figure 2. Roughly, the acidity of the acid component HX decreases from the top to the bottom. The stars and double stars characterize the hydrogen dicarboxylates (XHX^-) and

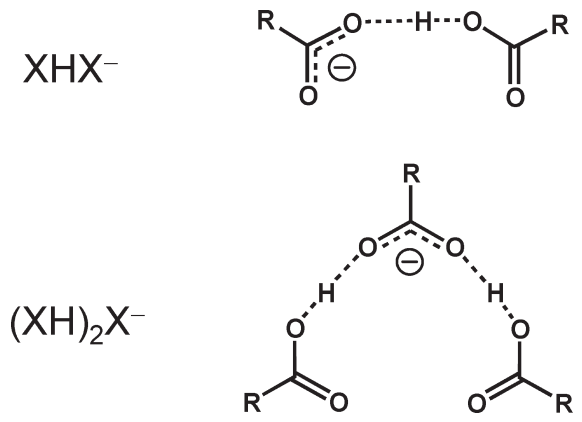

Figure 5. Chemical structures of (a) hydrogen dicarboxylate and (b) dihydrogen tricarboxylate. In this work, tetraethylammonim served as a countercation. The signals of hydrogen dicarboxylate and dihydrogen tricarboxylate are marked with * and **, respectively, in Figures 5, S2, and S3.

dihydrogen tricarboxylates $(XHXHX)^-$ whose structures are depicted in Figure 5. These structures have been characterized recently by ^{1}H and ^{13}C NMR in the cases of acetic acid and chloroacetic acid.[10] For reference we have included the spectra of free **2** as well as of 2-chloro-4-nitrophenol (**1**). The spectra were measured around 170−180 K. The full set of spectra is included in SI Figures S3−S6.

In the left column of Figure 4, the low-field parts of the ^{1}H NMR spectra are depicted. When the acidity of the added acid HX is decreased, the ^{1}H signal of the bridging proton of AHX^- is shifted to low field in the case of **4**−**14**; a maximum occurs around 19 ppm for **15**, and then the signal shifts to higher field again in the case of **16**−**27**. As the phenolic proton of **1** resonates around 7 ppm at 175 K,[29] the low-field ^{1}H NMR region of Figure 4a does not contain any signal.

The center column of Figure 4 depicts the corresponding UV−vis spectra between 270 and 500 nm of the chromophore moiety, 2-chloro-4-nitrophenol/2-chloro-4-nitrophenolate. These spectra were taken in the NMR spectrometer at the same time as the ^{1}H NMR spectra shown in the left column. As described in the Experimental Section, the samples had been prepared under NMR control in such a way that the UV−vis bands stem exclusively from single species involving the chromophore moiety. We note that XHX^- and $(XHXHX)^-$, which give rise to low-field ^{1}H NMR lines, do not absorb between 300 and 500 nm. The UV−vis absorption bands shown in Figure 4 and in SI Figures S5 and S6 arise from the electronic $\pi-\pi^*$ transitions of **1**, **2**, and the heteroconjugated 1:1 complexes **4**−**25**. A small contribution of **2** was taken into account in order to obtain the spectra of **26** and **27** as depicted in Figure S6. When the acidity of the acid component HX is decreased, a continuous red shift of the $\pi-\pi^*$ transition is observed. More on the shape of the UV−vis bands is given in the following subsection and in the Discussion.

The right column of Figure 4 contains the ^{13}C NMR signals of the 2-chloro-4-nitrophenolate/phenol moiety labeled with ^{13}C in the 1-C position, characterized by the chemical shift $\delta(\underline{C}OHX)$. ^{13}C NMR signals at natural abundance are not shown. The full set of ^{13}C NMR spectra is included in SI Figure S4. In the low-field part of ^{13}C NMR spectra (Figure 4, right), only the signals of the 1-C carbons of the 2-chloro-4-nitrophenolate/phenol moiety are visible, as only this position was enriched with ^{13}C. The spectra in Figure 4a and h feature signals at 155.9 and 173.9 ppm, respectively, stemming from neutral **1** and the anion **2**. The ^{13}C NMR spectra in Figure 4b−g have several signals, assigned to different complexes, as indicated by the numbers. Several species involving 2-chloro-4-nitrophenol might be present in solution, because, unlike for UVNMR measurements, the composition of the samples for ^{13}C NMR spectra was not optimized, such that the desired complex is the only species involving 2-chloro-4-nitrophenol formed at low temperatures. Additionally, after partial deuteration, most of the signals split into two, assigned to the nondeuterated ("H") and deuterated ("D") isotopologs of the complex, $\delta(\underline{C}OHX)$ and $\delta(\underline{C}ODX)$, respectively. The values $\delta(\underline{C}OHX)$ of the conjugated complexes vary in the range 157−171 ppm, having the chemical shifts $\delta(\underline{C}OH)$ and $\delta(\underline{C}O^-)$ as limits. The increasing values of $\delta(\underline{C}OHX)$ were used as a criterion for ordering all spectra, leading to the trends described above. There is an inversion in the sign of the secondary isotope effect on the 1-^{13}C chemical shifts, $\delta(\underline{C}ODX) - \delta(\underline{C}OHX)$, within the series.

The complete set of NMR and UV−vis data for all complexes studied, including the phenol **1** and its anion **2**, is assembled in Table 1.

UV−Vis Band Shape Analysis. An examination of the shapes of the UV−vis bands reveals the following features. At high and low energies single bands are observed, as illustrated by the spectra depicted in Figure 4a,b,g, and h. By contrast, dual bands are observed for complexes **11**, **13**, **15**, and **19** at intermediate energies (Figure 4c−f). In Figure 6, the experimental full widths at half-heights, $\Delta\tilde{\nu}$, are plotted versus the center of gravity of the band, $\tilde{\nu}_{COG}$. Starting on the high-energy side, we first observe for the single bands of **1** and **4**−**10** a monotonic decrease of the bandwidths with decreasing band energy. However, in the dual-band region, starting from complex **11** there is a sharp increase of $\Delta\tilde{\nu}$ that culminates for complex **15**, followed by a sharp decrease until complex **21**. Finally, a monotonic decrease is observed again for complexes **22**−**27** reaching a minimum for the anion **2**. The monotonic decrease of $\Delta\tilde{\nu}$ in both single-band regions is well described by the dashed line. The latter was used to represent the intrinsic bandwidths in the dual-band region. These bandwidths were then treated as fixed parameters of the log-normal function eq 1, used to simulate the blue and red components of the dual UV bands of Figure 4; only the band intensities and positions were varied until an optimal fit of the experimental spectra was obtained, leading to the superimposed experimental and calculated spectra in the center column of Figure 4. For clarity, the calculated individual bands are also included as dashed curves. Furthermore, we have represented each band by a vertical bar in Figure 4, located at the center of gravity, where the relative heights represent the band fractions given by

$$x_{blue} = \frac{A_{blue}}{A_{blue} + A_{red}}, \quad x_{red} = 1 - x_{blue} \qquad (2)$$

Here, A_{blue} and A_{red} are the integrated band intensities. In the case of the dual bands, the blue band dominates when a transition occurs at high energies, and the red band dominates when the transition occurs at low energies. The examples shown in Figure 4 hold for the full set of UV−vis spectra as depicted in SI Figures S5 and S6. All parameters of the UV band shape analyses are included in Table 1.

Table 1. Experimental ^{1}H and ^{13}C NMR Chemical Shifts and Parameters of the UV−Vis Absorption Bands of 1−27 in CD_2Cl_2 at 175 K[a]

	HX	δ(COHX)	δ(COHX)	δ(CODX)	$\tilde{\nu}_{COG}$	$\Delta\tilde{\nu}$	x_{blue}	$\tilde{\nu}_{blue}$	$\Delta\tilde{\nu}_{blue}$	$\tilde{\nu}_{red}$	$\Delta\tilde{\nu}_{red}$	q_1[b]	q_2[c]	r_{OH}[d]	Δr_{OH}[e]
1	–	6.70	155.9		33220	6000	1					−0.540	2.977	0.948	0.05
2	–		172.9		23540	2660	0								–
3	2-chloro-4-nitrophenol	18.54	165.5	165.40	27360	5410	0.28	30580	5310	26300	3850	−0.143	2.455	1.084	0.10
												0.143	2.455	1.370	0.15
4	hydrogen tetrafluoroborate	8.96	157.45	157.32	32230	5720	1	32230				−0.440	2.805	0.962	0.07
5	hydrogen iodide	9.81	157.91	157.76	31730	5650	1	31730				−0.410	2.757	0.968	0.08
6	hydrogen bromide	11.04	158.60	158.43	31570	5590	1	31570				−0.371	2.697	0.977	0.08
7	hydrogen chloride	12.29	159.22	159.02	31160	5460	1	31160				−0.333	2.643	0.989	0.09
8	trifluoroacetic acid	14.65	159.93	159.60	30690	5340	1	30690				−0.266	2.561	1.014	0.10
9	dichloroacetic acid	15.70	160.77	160.28	30200	5210	1	30200				−0.236	2.528	1.028	0.11
10	2,3,5-trichlorobenzoic acid	16.74	161.48	160.76	29880	5040	1	29880				−0.204	2.499	1.045	0.11
11	chloroacetic acid	17.35	162.06	161.15	29290	5330	0.81	29880	5110	27190	4190	−0.206	2.500	1.044	0.12
												0.025	2.416	1.233	0.14
12	3,5-dichlorobenzoic acid	18.26	162.84	161.79	28890	5530	0.76	29720	5070	26650	4050	−0.193	2.490	1.052	0.12
												0.076	2.426	1.289	0.14
13	formic acid	18.70	163.84	162.90	28270	6040	0.65	29490	4990	26420	3900	−0.173	2.474	1.064	0.12
												0.100	2.434	1.317	0.15
14	4-chlorobenzoic acid	19.02	164.61	163.84	27930	6240	0.58	29430	4940	26200	3820	−0.167	2.470	1.068	0.12
												0.124	2.445	1.346	0.15
15	benzoic acid	19.18	165.74	165.64	27530	6440	0.49	29370	4950	26050	3750	−0.162	2.467	1.071	0.12
												0.141	2.454	1.368	0.15
16	4-chlorophenylacetic acid	18.76	166.06	166.23	27260	6200	0.44	29300	4920	25930	3700	−0.156	2.463	1.075	0.12
												0.154	2.462	1.385	0.15
17	4-tert-butylbenzoic acid	19.11	166.37	166.66	27030	5880	0.42	29020	4830	25810	3660	−0.132	2.449	1.092	0.13
												0.168	2.471	1.403	0.15
18	phenylacetic acid	18.68	166.68	167.20	26890	5750	0.40	28970	4820	25730	3620	−0.129	2.447	1.095	0.13
												0.179	2.479	1.418	0.15
19	3-phenylpropionic acid	18.43	167.74	168.64	26390	4810	0.29	28900	4800	25550	3550	−0.123	2.444	1.099	0.13
												0.202	2.497	1.450	0.16
20	acetic acid	18.16	168.15		26310	4600	0.26	29040	4840	25500	3530	−0.134	2.450	1.091	0.13
												0.208	2.502	1.459	0.16
21	4-phenylbutyric acid	17.98	168.43	169.42	25910	4080	0.18	28730	4740	25390	3480	−0.108	2.437	1.110	0.13
												0.224	2.517	1.482	0.16
22	pivalic acid	17.47	169.05	169.93	25450	3750	0			25450		0.181	2.480	1.421	0.20
23	2,4,5-trichlorophenol	16.53	169.36	170.04	25590	3590	0			25590		0.211	2.505	1.463	0.16
24	4-nitrophenol	16.49	169.48	170.16								0.212	2.506	1.465	
25	2,4-dichlorophenol	15.40	170.08	170.48	25321	3470	0			25321		0.244	2.536	1.512	0.16
26	4-chlorophenol	13.70	170.73	170.92	24911	3110	0			24911		0.293	2.592	1.589	0.12
27	4-methylphenol	12.86	171.20	171.41	24836	3190	0			24836		0.317	2.622	1.628	0.15

[a] Chemical shifts δ in ppm. Distances q_1 and r_{OH} in Å. Wave numbers in cm^{-1}. $\tilde{\nu}_{COG}$, center of gravity of single or dual bands; $\tilde{\nu}_{blue}$ and $\tilde{\nu}_{red}$, centers of gravity of the dual bands; $\Delta\tilde{\nu}_{COG}$, experimental bandwidths; $\Delta\tilde{\nu}_{blue}$ and $\Delta\tilde{\nu}_{red}$, corresponding bandwidths calculated using the log normal function of eq 1. [b] Single values of q_1 were calculated from δ(COHX) using eq 4. Pairs of q_1 values: the upper (lower) values were obtained by fitting $\tilde{\nu}_{blue}$ ($\tilde{\nu}_{red}$) to the dashed correlation curve in Figure 9b. [c] Values corresponding to the dotted curve in Figure 9a. [d] Calculated from the dotted curve in Figure 9a. [e] Width of the distribution of O···H distances, estimated according to Figure 9c.

DISCUSSION

The purpose of the present study was to elucidate how the UV absorption frequencies and important NMR parameters of hydrogen-bonded 1:1 complexes AHX^- of the chromophore AH = 2-chloro-4-nitrophenol (**1**) with various anions X^- (Figure 2) behave when H is shifted away from the phenol oxygen to the anion. In particular, we have studied the ^{1}H and ^{13}C chemical shifts as well as the H/D isotope effects on the ^{13}C chemical shifts of the hydrogen bridges COHX of AHX^-, where C represents the carbon position C-1 of AH. The experiments were performed using CD_2Cl_2 as solvent around 175 K. Indeed, we find typical changes in the NMR as well as in the UV spectra, which together provide novel information about the proton-transfer pathways, as will be discussed in the following. In particular, in the case of complexes AHX^- exhibiting strong hydrogen bonds, we observe dual UV−vis bands (Figure 4) indicating the presence of two tautomeric forms, whereas the NMR spectra provide NMR parameters averaged over both forms.

dx.doi.org/10.1021/ja201113a |J. Am. Chem. Soc. 2011, 133, 7897–7908

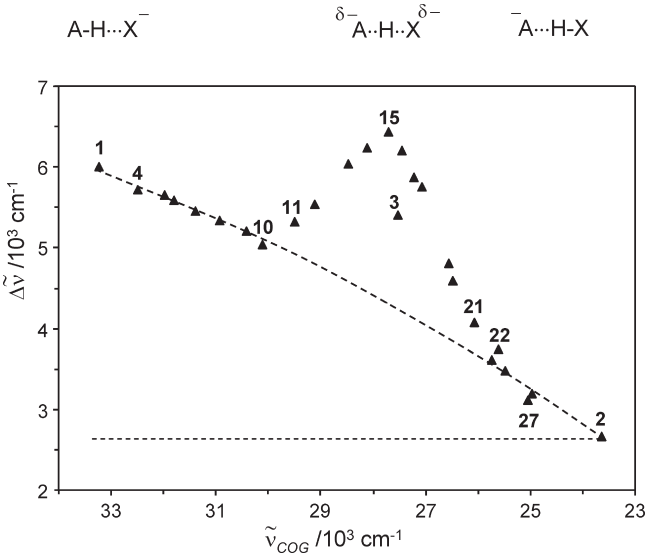

Figure 6. Experimental full width at half-height of $\pi-\pi^*$ absorption band of neutral **1**, its anion **2**, and conjugate complexes of **3**−**27**, measured in CD_2Cl_2 solution at 170−180 K, plotted versus the center of gravity of the whole band. The dashed line represents a second-order polynomial fit to the data of species **1**, **2**, **4**−**10**, **22**−**27** that follow a monotonic decrease in bandwidth against decreasing transition energy.

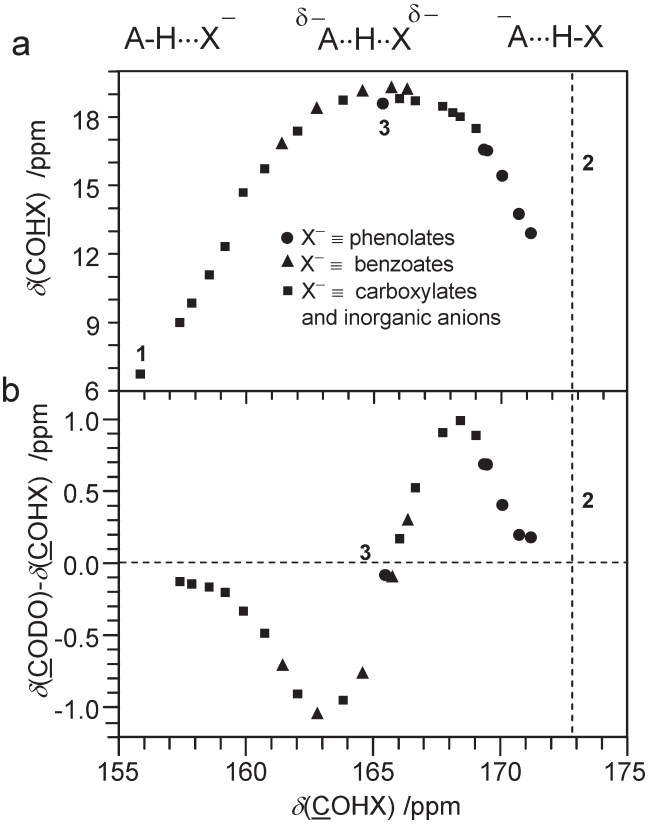

Figure 7. Experimental NMR parameters of 2-chloro-4-nitrophenol (**1**) and its conjugated anions **3**−**27** (see Table 1) plotted as a function of the ^{13}C chemical shift $\delta(\underline{C}OHX)$ of C-1 of **1**. (a) ^1H chemical shift of bridging proton $\delta(CO\underline{H}X)$. (b) H/D isotope effect $\delta(\underline{C}ODX) - \delta(\underline{C}OHX)$. Triangles refer to complexes where the partner of **1** is a benzoate, circles where the partner is a phenolate. In other cases the symbol is a square. The vertical dashed line corresponds to the anion **2**.

NMR Parameter Correlations. Let us first discuss the NMR parameters of AHX^-. In Figure 7a the chemical shifts $\delta(CO\underline{H}X)$ of the hydrogen-bonded protons are plotted as a function of the ^{13}C chemical shift $\delta(\underline{C}OHX)$ of the phenolic carbon C-1. $\delta(\underline{C}OHX)$ provides a convenient measure of the proton position. The data points of the complexes with HX = benzoic acids are symbolized by triangles, those with HX = phenols by circles, and those with the remaining saturated carboxylic and inorganic acids as well as neutral **1** by squares. These symbols will be used also in the following figures.

The vertical dashed line represents the free anion **2**, providing the limiting ^{13}C chemical shift in the absence of a mobile proton. An excellent bell-shaped correlation is observed. Neutral **1** exhibits the lowest ^1H chemical shift of 7 ppm, corresponding to the average value of weakly hydrogen-bonded self-associates. We expect the free **1** to resonate at higher fields in view of the finding that, for nonsubstituted phenol in the gas phase at 422 K, a value of 3.77 ppm with respect to gaseous TMS has been reported.[35] Dilution experiments revealed chemical shifts of 4.29 ppm for monomeric phenol and 5.16 ppm for 4-nitrophenol in carbon tetrachloride.[36] For given values of $\delta(\underline{C}OHX)$, the proton chemical shifts $\delta(CO\underline{H}X)$ seem to be slightly larger for complexes with benzoates as partners than for complexes with carboxylates. We further note that the value of $\delta(CO\underline{H}X)$ of the homoconjugated complex **3** is 18.5 ppm, slightly smaller than those of several heteroconjugated complexes; the maximum chemical shift of 19.2 ppm is obtained for **15**. These values are, in turn, smaller than the ones of ∼20−21 ppm obtained for the strongest OHO hydrogen bonds[9] and indicate the absence of extremely strong symmetric hydrogen bonds. Below it will be shown that these findings are consistent with the occurrence of double bands in UV−vis.

In Figure 7b, the secondary H/D isotope effect on carbon chemical shift, $\delta(\underline{C}ODX) - \delta(\underline{C}OHX)$, is plotted as a function of $\delta(\underline{C}OHX)$. A dispersion-shaped correlation is observed, changing sign when the bell-shaped correlation curve of Figure 7a exhibits its maximum. These findings indicate that $\delta(\underline{C}OHX)$ increases monotonically when H is shifted away from the phenolic oxygen. Whereas different chemical substitution does not seem to play a major role, we note that it is important to compare only data observed using the same solvent and similar temperatures. Finally, we note that similar dispersion-shaped curves have been observed previously in the case of H/D isotope effects on heavy-atom chemical shifts of various hydrogen-bonded complexes of carboxylic acids.[16]

An additional correlation is observed between the values of $\delta(\underline{C}OHX)$ and the chemical shifts of the protons H-6 of the 2-chloro-4-nitrophenol moiety. This signal had been used in the adjustment of sample composition as described in the Experimental Section. For further details we refer the reader to SI Figure S7 and the accompanying text.

UV−Vis/NMR Correlation. In Figure 8a we have plotted the UV−vis band frequencies of the $\pi-\pi^*$ transitions of the systems studied as a function of the corresponding ^{13}C chemical shifts, $\delta(\underline{C}OHX)$. The filled symbols, $\tilde{\nu}_{COG}$ (or λ_{COG}), represent the experimental centers of gravity of the UV−vis bands. We observe a linear correlation between $\tilde{\nu}_{COG}$ and the chemical shift of the phenolic carbon $\delta(\underline{C}OHX)$. Thus, the values of $\tilde{\nu}_{COG}$ represent measures for the H-bond geometries as the chemical shifts, where the averaging is performed in both cases over all possible

dx.doi.org/10.1021/ja201113a |J. Am. Chem. Soc. 2011, 133, 7897–7908

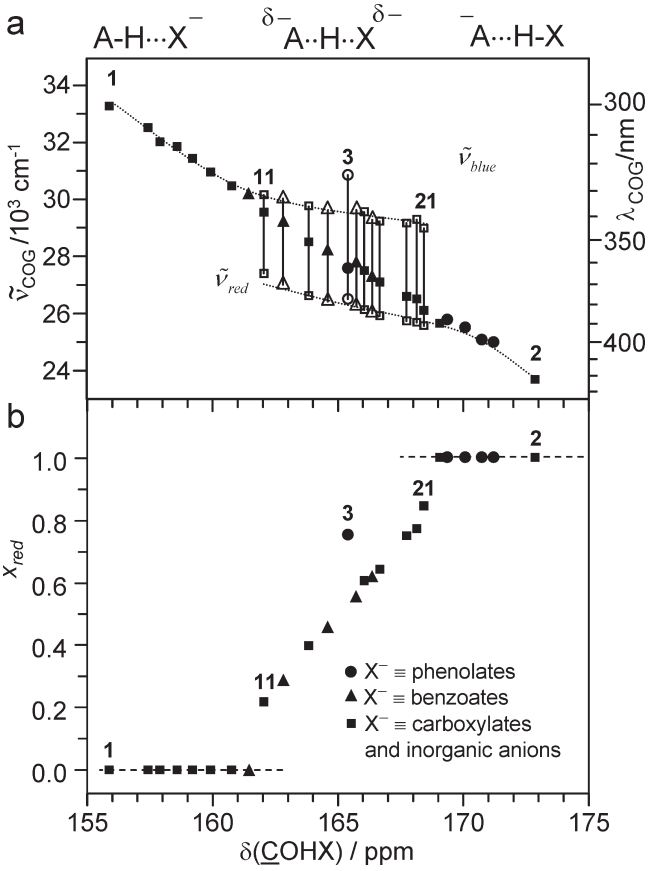

Figure 8. NMR and UV−vis parameters of the $\pi-\pi^*$ transition of 2-chloro-4-nitrophenol (**1**), its anion **2**, and its conjugated anions **3**−**27** (see Table 1). (a) Center of gravity of the experimental absorption band (solid symbol) and centers of gravity of log-normal fit functions (open symbols) obtained as explained in the text versus the ^{13}C chemical shift of C-1. (b) Fraction x_{red} of integral area of the "red band" fit function (for more details see text).

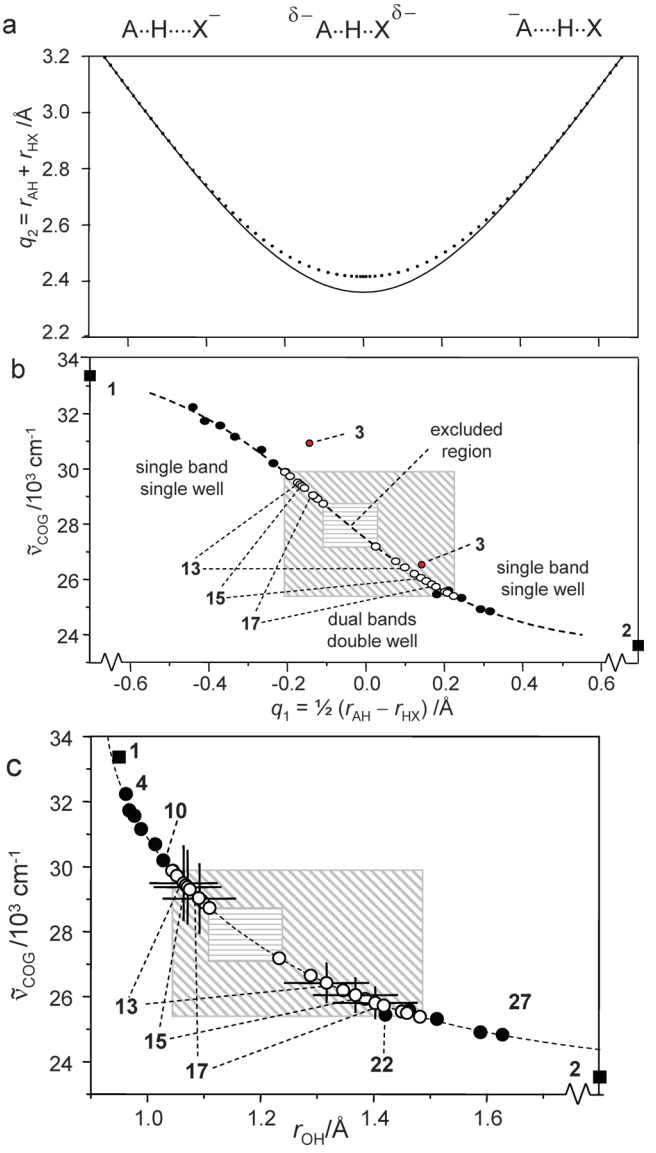

Figure 9. (a) Hydrogen bond correlation q_2 vs q_1 of OHO hydrogen bonds in the solid state, adapted from ref 9. The solid line refers to equilibrium geometries. The dotted line represents an empirical correction for anharmonic zero-point vibrations. (b) Center of gravity of the experimental absorption band plotted versus the H-bond coordinate q_1 estimated using eq 5. The data points corresponding to the UV−vis spectra for which fitting with a single log-normal band (solid symbols) and two log-normal bands (open symbols) was done are plotted. The meaning of the shadowed areas is explained in the text. (c) Center of gravity of the experimental absorption band plotted versus the r_{OH} distance in a similar way as in (b). Error bars illustrate the width of inhomogeneous distribution of r_{OH} estimated from the experimental UV−vis bandwidths.

tautomers, potential wells, or solvent configurations. However, whereas the averaging is dynamic in the case of NMR, the UV−vis bands contain information about the distribution of H-bond geometries.

When H is close to A or close to X, single UV−vis bands are observed, depending on the relative basicities of A^- and of X^-. Thus, in these cases only single wells of the type A−H···X^- or A^-···H−X are observable. By contrast, at intermediate basicities, strong and short hydrogen bonds are formed, as indicated by the low-field ^1H NMR shifts; in this region, dual UV−vis bands are observed. The centers of gravity of each sub-band, $\tilde{\nu}_{blue}$ of the blue component and $\tilde{\nu}_{red}$ of the red component, are depicted in Figure 8a by open symbols. We note that in the dual-band region $\tilde{\nu}_{blue}$ and $\tilde{\nu}_{red}$ are not constant but decrease slightly when δ(COHX) is increased.

The fraction $x_{red} = 1 - x_{blue}$ of the red components obtained by band shape analysis is depicted in Figure 8b as a function of δ(COHX). When H is close to A, x_{red} is zero but increases monotonically to a value of 1 in the dual-band region. Later, we will interpret these findings in terms of an equilibrium between two tautomeric forms, A−H···X^- and A^-···H−X.

The only data point that deviates somewhat from the correlations in Figure 8 arises from the homoconjugated anion **3**, in which the red band component dominates, and where the blue band appears at a higher energy than expected by extrapolation of the data of the heteroconjugated complexes. On the other hand, the center of gravity of the experimental band, $\tilde{\nu}_{COG}$, represented by the solid circle located centrally in Figure 8a does not differ substantially from the linear correlation with δ(COHX).

As illustrated in SI Figure S8 (see also Table S2), using the frequencies of the absorption maxima instead of centers of gravity would lead to similar results besides a constant red-shift of about 500 cm^{-1}.

dx.doi.org/10.1021/ja201113a |J. Am. Chem. Soc. 2011, 133, 7897–7908

UV−Vis/Hydrogen Bond Correlation. In order to interpret the spectroscopic changes of AHX^- upon increasing the basicity of X^- in terms of the proton-transfer pathway from A to X, we use H-bond correlations established previously using neutron and NMR crystallography as well as computational methods.[3−9] The main result of these correlations is that the two distances, r_{AH} and r_{HX}, of a hydrogen bridge or their combinations are correlated with each other.

$$q_1 = (r_{AH} - r_{HX})/2, \quad q_2 = r_{AH} + r_{HX} \tag{3}$$

In the case of linear hydrogen bonds, the proton coordinate q_1 (in Å) represents the distance of H from the H-bond center and q_2 (in Å) the heavy-atom distance. The correlation is depicted in Figure 9a for the case of OHO hydrogen bonds.[9] When H is transferred through the H-bond center, i.e., q_1 is changed from negative to positive values, q_2 is decreased and increased again, exhibiting a minimum when H is located in the H-bond center at $q_1 = 0$. The solid line refers to equilibrium structures where H is considered as a point in space. The dotted line refers to a correction for the shape of the proton. Due to anharmonic zero-point vibrations, the volume of the proton is not zero, and hence the shortest heavy -atom distance cannot be achieved. For details of the mathematical relations between q_1 and q_2, the reader is referred to ref 9.

Using solid-state NMR, a simple relation between ^{1}H chemical shifts and q_1 of OHO hydrogen bonds has been proposed which we use to estimate average H-bond geometries of complexes studied here,[9]

$$\delta(\mathrm{CO}\underline{H}\mathrm{X}) = \delta_o + \Delta \exp(-6.2{q_1}^2) \tag{4}$$

where the maximum shift is $\delta_o + \Delta = 20.5$ ppm, independent of the chemical environment. δ_o refers to the free proton donor whose chemical shift depends, on the other hand, on the chemical environment. Thus, for water and aliphatic hydroxyl groups, $\delta_o \approx 0.7$ ppm, whereas 6 ppm was calculated for free carboxylic acids. In the cases of the phenols studied here, we estimate $\delta_o = 4$ ppm, derived from the value of the free phenol monomer.[35,36]

Using the experimental ^{1}H chemical shifts, we have calculated in a first stage the values of q_1 for the systems exhibiting a single UV−vis band. The data points are included in Table 1, together with those of q_2 and r_{OH}. In Figure 9b, we have plotted the UV−vis band positions as a function of the values of the proton coordinate q_1, leading to the data points symbolized by the solid circles. They indicate a correlation which could be expressed by the dashed sigmoidal curve corresponding to the empirical equation

$$\tilde{\nu} = 23500 + 10500/\left(\exp\left(\frac{q_1 + 0.11}{0.22}\right) + 1\right) \tag{5}$$

where $\tilde{\nu}$ is in cm^{-1} and q_1 is in Å. We have included the data points of neutral **1** and of the anion at infinite negative and positive values of q_1 from which the two wave numbers in eq 5 were estimated. When the proton is far away from the H-bond center, the band positions do not change with q_1, but they change strongly when the proton goes through the H-bond center. In Figure 9c we have transformed the abscissa to the distance r_{OH}. When H is located near the chromophore, i.e., if the latter is neutral and r_{OH} small, changes of r_{OH} induce large changes of the UV band frequencies. By contrast, as expected, when the chromophore carries the negative charge and r_{OH} is large, the band positions are less affected by changes of the proton position. The other features of Figure 9c are similar to those of Figure 9b, besides the vertical and horizontal "distribution bars" which we have included for some of the data points arising from the dual-band region. These bars will be discussed below in more detail.

The region of the dual bands which most likely indicate the presence of two tautomers was analyzed as follows. The "blue" ("red") band arises from the tautomer with the hydrogen-bonded proton closer to (farther away from) the phenol chromophore. We used then eq 5 and the equations of ref 9 to calculate the values of q_1 and of r_{OH} of the tautomer pairs from the values of $\tilde{\nu}_{blue}$ and $\tilde{\nu}_{red}$. The resulting data points are shown in Figure 9b,c by open circles, located exactly on the dashed correlation curve. All data are included in Table 1. The tautomer pairs are identified in a couple of cases in Figure 9b,c by broken lines.

We note that dual bands, i.e., tautomerism, occur in the range $-0.2 < q_1 < +0.2$ Å or $1.05 < r_{OH} < 1.50$ Å, as symbolized in Figure 9b,c by the diagonally hatched areas. On the other hand, a region where H-bond geometries are excluded is illustrated by the horizontally hatched areas $-0.1 < q_1 < +0.05$ Å or $1.1 < r_{OH} < 1.25$ Å.

UV Bandwidth and Distribution of Hydrogen Bond Geometries. Before we discuss the implications of these findings, let us first discuss how a distribution of H-bond geometries will influence the UV−vis bands. A distribution arises from a number of different solvent configurations, as has been suggested previously for a series of neutral complexes with OHN hydrogen bonds.[19] The latter have also been called "solvatomers".[20] As the UV band frequencies depend on the H-bond geometries, a distribution of the latter should lead to inhomogeneously broadened UV−vis bands if the interconversion of the different configurations is slow on the UV time scale. Indeed, the observed decrease of the bandwidths $\Delta\tilde{\nu}$ depicted in Figure 6 can be consistently explained in this way.

For that purpose we have introduced in Figure 9c vertical and horizontal "distribution bars" for some of the data points arising from the dual-band region. In order to derive these bars we proceeded as follows. We noticed that the experimental bandwidth $\Delta\tilde{\nu}(\mathbf{2})$ of the anion **2** is particularly small, as illustrated in Figure 4h, which could arise from the fact that there is no hydrogen-bonded proton close to the chromophore. Hence, $\Delta\tilde{\nu}(\mathbf{2})$is not affected by H-bond geometries. Thus, we assume that the contribution $\Delta\tilde{\nu}_d(i)$ for complex i from the H-bond distribution can be estimated from the difference

$$\Delta\tilde{\nu}_d(i) = \Delta\tilde{\nu}(i) - \Delta\tilde{\nu}(\mathbf{2}) \tag{6}$$

where $\Delta\tilde{\nu}(i)$ represents the observed bandwidth of complex i, assembled in Table 1. Thus, all other broadening mechanisms, including nonresolved vibronic transitions and phonon side bands as well as their interconversion by spectral diffusion, are then included in $\Delta\tilde{\nu}(\mathbf{2})$. Further discussion of this quantity is beyond the scope of this study. $\Delta\tilde{\nu}_d(i)$ values are collected in SI Table S2.

The values of $\Delta\tilde{\nu}_d(i)$ were introduced into Figure 9c as vertical distribution bars. The horizontal distribution bars Δr_{OH} could then be calculated from the dashed correlation curve. The values are included in Table 1. The graph shows that a distribution width Δr_{OH} leads to a small contribution to the inhomogeneous broadening of the UV bandwidth when r_{OH} is large, but to a substantial broadening when r_{OH} is small. From the graph it follows that the Δr_{OH} increases slightly when r_{OH} is increased, although the bandwidth decreases.

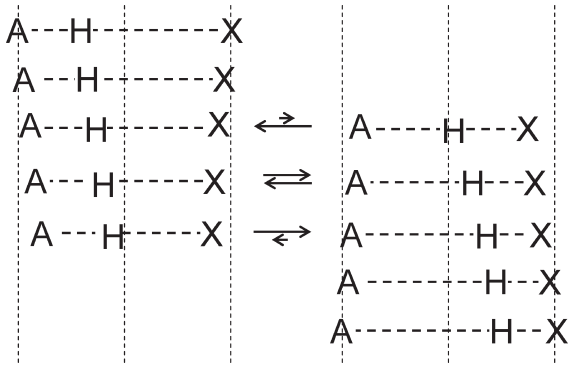

Figure 10. Schematic representation of the proton-transfer pathway combining geometrical shifts and population distribution in a two-state approximation found in this work for conjugate anions of 2-chloro-4-nitrophenol. Negative charges have been omitted.

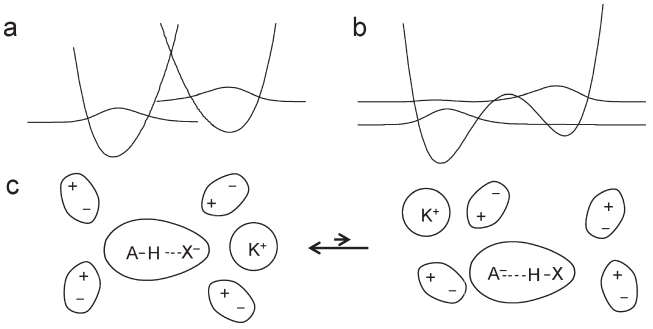

Figure 11. (a) Diabatic potential for the tautomerism in a strong hydrogen bond. (b) Adiabatic double-well potential. (c) Schematic illustration of the different organization of the countercation K^+ and the solvent dipoles around a negatively charged hydrogen-bonded anion exhibiting a two-state tautomerism.

In conclusion, we can understand qualitatively the monotonic increase of the bandwidth in Figure 4 when the basicity of the accepting anion is decreased. Moreover, neutral **1** exhibits a particularly large bandwidth. This can then be explained in terms of a distribution of hydrogen-bonded associates containing a varying number of molecules, resulting in slightly different distances r_{OH}.

Proton-Transfer Pathways Elucidated by UVNMR. The results described above are summarized schematically in Figure 10. When H is located near A, i.e., the acidity of AH or the basicity of X small, a single tautomer is formed (Figure 10, top). When the acidity of AH or the basicity of X is increased, H is shifted toward the H-bond center and the hydrogen bond is compressed, i.e., the A···X distance decreases. At a certain point, a second tautomer appears (Figure 10, center) which becomes more and more populated. The bridging proton positions in both tautomers shift monotonically toward the acceptor X. At the same time, the A···X distance decreases in the tautomer A−H···X^- and increases in A^-···H−X. Finally, the second tautomer survives alone, but its structure continues to change in a monotonic way (Figure 10, bottom).

The geometry range in which the tautomerism occurs is surprisingly small and confined to values of q_1 between about −0.2 and 0.2 Å, as illustrated by the diagonally hatched area in Figure 9b. This corresponds to values of q_2, i.e. to A···X distances between 2.5 and 2.4 Å, and i.e. to the shortest and strongest OHO hydrogen bonds. Moreover, the geometric region without any tautomer is confined to values of q_1 between only about −0.10 and 0.05 Å, as illustrated by the horizontally hatched area in Figure 9b. These values are comparable with the width of the square of the vibrational wave function of the proton. Neutron structures of strong hydrogen bonds indicate an even larger "width" of at least 0.5 Å.[37] Thus, the tautomerism is not a normal one as expected for a simple reaction, as was illustrated in Figure 1b. Usually, the equilibrium between the two forms is characterized by an equilibrium constant of tautomerism. However, that requires a diabatic potential for the proton motion, as illustrated schematically in Figure 11a. In this case, both tautomers exhibit individually different electronic transitions, different H-bond geometries, and well distinct partition functions. On the other hand, an adiabatic potential may also be realized. One possible configuration is illustrated in Figure 11b. A series of adiabatic potentials along the proton-transfer pathway has been proposed by Hynes et al.[38] In this case, because of the small barrier, the partition functions of both tautomers are entangled, and the interpretation of the dual-absorption bands in terms of two different tautomers may break down.

In all cases, solvent reorientation will play an important role. Thus, it is conceivable that a given tautomer is associated with a range of given solvent configurations, as illustrated schematically in Figure 11c. Around the moiety exhibiting the negative charge, e.g., X^-, the countercation K^+ will be located and the solvent dipoles will exhibit a higher ordering than around the neutral chromophore AH. The opposite will be true if the chromophore carries the negative charge. In the wording proposed by Perrin et al.,[20] each tautomer will exhibit a given subset of "solvatomers", leading to a diabatic potential for the tautomerism.

The interpretation of our findings in terms of a two-state tautomerism is not in disagreement with H-bond correlations described by some of us previously, which have been applied not only to solids but also to liquids.[7−9] In the latter case, the distances used in the correlations represent averages over all solvent configurations and possible tautomers. On the other hand, our findings support the finding of Perrin et al.,[20] who showed using isotope NMR methods that the symmetry of potentially symmetric hydrogen bonds is lifted in the liquid state.

This leads us to the problem of the homoconjugate anion **3** (AHA^-). From the ^{1}H chemical shift correlation of eq 4, we obtain for the proton chemical shift of 18.5 ppm the values $q_1 = \pm 0.143$ Å, which indicates the presence of a degenerate tautomerism between two forms or a symmetric double well. This is confirmed by the observation of a dual band. Whereas $\tilde{\nu}_{red}$ is located near the dashed correlation curve in Figure 9b, the value of $\tilde{\nu}_{blue}$ is substantially larger than predicted. This means that the two chromophores interact strongly with each other, despite their significant nonequivalence. Further theoretical studies will be necessary to describe the combined UV−vis/NMR results of this system in the future.

■ CONCLUSIONS

The main result of this study is the finding that the UV−vis band frequencies of a phenolic chromophore forming OHO hydrogen bonds with proton acceptors are correlated with averaged NMR parameters such as ^{1}H and ^{13}C chemical shifts and H/D isotope effects on the latter. As in previous work,[7,9,16] in which some of us had established correlations of NMR parameters with H-bond geometries, the new results indicate a

correlation of the UV−vis band frequencies with the O···H distances, a result which had not previously been recognized. The advantage of UV−vis spectroscopy is that different H-bond configurations are in slow exchange. Hence, once the samples have been characterized by NMR, UV−vis provides information about whether the proton motion involves single or double wells and how H-bond configurations are influenced by the solvent. In the case of weaker hydrogen bonds, we observed single UV bands indicating the occurrence of single wells for the proton motion. By contrast, dual bands were observed for strong and short hydrogen bonds, indicating the presence of two configurations, i.e., tautomeric states. As a consequence, the inhomogeneous part of the UV−vis bands provides evidence about the distribution of H-bond geometries. These findings may be important in the interpretation of UV−vis shifts after irradiation of phenolic chromophores in proteins such as the photoactive yellow protein[28] with light. A quantitative treatment of the correlations of the above-mentioned spectroscopic parameters with H-bond geometry, based on existing quantitative relationships, is pending and will be published elsewhere. In any case, the experimental results obtained in this study may require further theoretical studies.

■ ASSOCIATED CONTENT

Supporting Information. Sample composition (types A and B) as determined by ^{1}H NMR and ratios $n(HX)/n(X^-)$ for type A samples; schematics of UVNMR sample tubes; complete set of low-field parts of ^{1}H NMR, ^{13}C NMR, and UV−vis spectra for complexes **1**−**27**; wavelengths of the UV−vis bands' maxima, centers of gravity, and bandwidths as well as the ^{1}H NMR chemical shifts of the *ortho* protons of the chromophore for complexes **1**−**27**; and comparison of the position of ^{1}H NMR signals of complexes **3**−**22** and **24**−**27** for type A and type B samples. This material is available free of charge via the Internet at http://pubs.acs.org.

■ AUTHOR INFORMATION

Corresponding Author
tolstoy@chemie.fu-berlin.de

Present Addresses
[§]Max Born Institut für Nichtlineare Optik and Kurzzeitspektroskopie, Max-Born-Strasse 2A, D-12489 Berlin, Germany

■ ACKNOWLEDGMENT

We thank Dr. E. T. J. Nibbering, Max-Born Institute, Berlin, and Prof. G. S. Denisov, St. Petersburg State University, as well as Prof. Maurice Kreevoy, Minneapolis, for helpful discussions. This work has been supported by the Deutsche Forschungsgemeinschaft, Bonn, the Fonds der Chemischen Industrie, Frankfurt, the Russian Foundation of Basic Research, and the European Research Council under the European Union's Seventh Framework Program (FP7/2007-2013/ERC grant agreement no. 247051 T.E.).

■ REFERENCES

(1) *Isotope Effects in Chemistry and Biology*; Kohen, A., Limbach, H. H., Eds.; Taylor & Francis: Boca Raton, FL, 2006.

(2) *Hydrogen Transfer Reactions*; Hynes, J. T., Klinman, J., Limbach, H. H., Schowen, R. L., Eds.; Wiley-VCH: Weinheim, 2007; Vols. 1−4.

(3) (a) Steiner, Th.; Saenger, W. *Acta Crystallogr.* **1994**, *B50*, 348–357. (b) Steiner, Th. *J. Chem. Soc., Chem. Commun.* **1995**, 1331–1332. (c) Gilli, P.; Bertolasi, V.; Ferretti, V.; Gilli, G. *J. Am. Chem. Soc.* **1994**, *116*, 909–915. (d) Steiner, Th. *J. Phys. Chem. A* **1998**, *102*, 7041–7052.

(4) (a) Benedict, H.; Limbach, H. H.; Wehlan, M.; Fehlhammer, W. P.; Golubev, N. S.; Janoschek, R. *J. Am. Chem. Soc.* **1998**, *120*, 2939–2950. (b) Lorente, P.; Shenderovich, I. G.; Golubev, N. S.; Denisov, G. S.; Buntkowsky, G.; Limbach, H. H. *Magn. Reson. Chem.* **2001**, *39*, S18–S29.

(5) Ramos, M.; Alkorta, I.; Elguero, J.; Golubev, N. S.; Denisov, G. S.; Benedict, H.; Limbach, H. H. *J. Phys. Chem. A* **1997**, *101*, 9791–9800.

(6) Smirnov, S. N.; Golubev, N. S.; Denisov, G. S.; Benedict, H.; Schah-Mohammedi, P.; Limbach, H. H. *J. Am. Chem. Soc.* **1996**, *118*, 4094–4101.

(7) Limbach, H. H.; Denisov, G. S.; Golubev, N. S. In *Isotope Effects in Chemistry and Biology*; Kohen, A., Limbach, H. H., Eds.; Taylor & Francis: Boca Raton, FL, 2006; pp 193−230.

(8) Tolstoy, P. M.; Schah-Mohammedi, P.; Smirnov, S. N.; Golubev, N. S.; Denisov, G. S.; Limbach, H. H. *J. Am. Chem. Soc.* **2004**, *126*, 5621–5634.

(9) Limbach, H. H.; Tolstoy, P. M.; Pérez-Hernández, N.; Guo, J.; Shenderovich, I. G.; Denisov, G. S. *Isr. J. Chem.* **2009**, *49*, 199–216.

(10) (a) Sternberg, U.; Brunner, E. *J. Magn. Reson. A* **1994**, *108*, 142–150. (b) Harris, T. K.; Zhao, Q.; Mildvan, A. S. *J. Mol. Struct.* **2000**, *552*, 97–109.

(11) Jeffrey, G. A.; Yeon, Y. *Acta Crystallogr. B* **1986**, *B42*, 410–413.

(12) Shenderovich, I. G.; Limbach, H. H.; Smirnov, S. N.; Tolstoy, P. M.; Denisov, G. S.; Golubev, N. S. *Phys. Chem. Chem. Phys.* **2002**, *4*, 5488–5497.

(13) Shenderovich, I. G.; Tolstoy, P. M.; Golubev, N. S.; Smirnov, S. N.; Denisov, G. S.; Limbach, H. H. *J. Am. Chem. Soc.* **2003**, *125*, 11710–11720.

(14) Detering, C.; Tolstoy, P. M.; Golubev, N. S.; Denisov, G. S.; Limbach, H. H. *Dokl. Phys. Chem.* **2001**, *379*, 1–4.

(15) Schah-Mohammedi, P.; Shenderovich, I. G.; Detering, C.; Limbach, H. H.; Tolstoy, P. M.; Smirnov, S. N.; Denisov, G. S.; Golubev, N. S. *J. Am. Chem. Soc.* **2000**, *122*, 12878–12879.

(16) Tolstoy, P.; Guo, J.; Koeppe, B.; Golubev, N.; Denisov, G.; Smirnov, S.; Limbach, H. H. *J. Phys. Chem. A* **2010**, *114*, 10775–10782.

(17) Gu, Z.; Zambrano, R.; McDermott, A. *J. Am. Chem. Soc.* **1994**, *116*, 6368–6372.

(18) (a) Sharif, S.; Denisov, G. S.; Toney, M. D.; Limbach, H. H. *J. Am. Chem. Soc.* **2007**, *129*, 6313–6327. (b) Sharif, S.; Denisov, G. S.; Toney, M. D.; Limbach, H. H. *J. Am. Chem. Soc.* **2006**, *128*, 3375–3387. (c) Sharif, S.; Fogle, E.; Toney, M. D.; Denisov, G. S.; Shenderovich, I. G.; Tolstoy, P. M.; Chan-Huot, M.; Buntkowsky, G.; Limbach, H. H. *J. Am. Chem. Soc.* **2007**, *129*, 9558–9559.

(19) Golubev, N. S.; Denisov, G. S.; Smirnov, S. N.; Shchepkin, D. N.; Limbach, H. H. *Z. Phys. Chem.* **1996**, *196*, 73–84.

(20) Perrin, C. L.; Lau, J. S. *J. Am. Chem. Soc.* **2006**, *128*, 11820–11824.

(21) Perrin, C. L. *Acc. Chem. Res.* **2010**, *43*, 1550–1557.

(22) (a) Nagakura, S.; Baba, H. *J. Am. Chem. Soc.* **1952**, *74*, 5693–5698. (b) Baba, H.; Suzuki, S. *J. Chem. Phys.* **1961**, *35*, 1118–1127. (c) Baba, H.; Suzuki, S. *J. Chem. Phys.* **1963**, *38*, 349–353.

(23) (a) Bell, C. L.; Barrow, G. M. *J. Chem. Phys.* **1959**, *31*, 1158–1163. (b) Baba, H.; Matsuyama, A.; Kokubun, H. *J. Chem. Phys.* **1964**, *41*, 895–896. (c) Baba, H.; Matsuyama, A.; Kokubun, H. *Spectrochim. Acta* **1969**, *25A*, 1709–1722. (d) Hudson, R. A.; Scott, R. M.; Vinogradov, S. N. *J. Phys. Chem.* **1972**, *76*, 1989–1993. (e) Romanowski, H.; Sobczyk, L. *J. Phys. Chem.* **1975**, *79*, 2535–2542.

(24) Kreevoy, M. M.; Liang, T. M. *J. Am. Chem. Soc.* **1980**, *102*, 3315–3322.

(25) (a) Magonski, J. *J. Solution Chem.* **1990**, *19*, 597–607. (b) Magonski, J. *J. Phys. Org. Chem.* **2002**, *15*, 204–210.

(26) (a) Pawlak, Z.; Magonksi, J.; Jasinski, T. *J. Mol. Struct.* **1978**, *47*, 329–338. (b) Pawlak, Z.; Magonksi, J. *J. Mol. Struct.* **1980**,

60, 179–185. (c) Magonksi, J.; Pawlak, Z. *J. Mol. Struct.* **1982**, *80*, 243–250.

(27) Anderson, S.; Crosson, S.; Moffat, K. *Acta Crystallogr. D* **2004**, *60*, 1008–1016.

(28) Joshi, C. P.; Otto, H.; Hoersch, D.; Meyer, T. E.; Cusanovich, M. A.; Heyn, M. P. *Biochemistry* **2009**, *39*, 9980–9993.

(29) Tolstoy, P. M.; Koeppe, B.; Denisov, G. S.; Limbach, H. H. *Angew. Chem., Int. Ed.* **2009**, *48*, 5745–5747.

(30) Drehmann, U.; Pürschel, U.; Wauschkun, H. *J. Prakt. Chem.* **1961**, *14*, 122–126.

(31) Fanta, P. *Org. Synth.* **1952**, *32*, 95–96.

(32) Ermakov, A. A.; Ermakov, S. A.; Polomarchuk, N. I. Russian Patent RU 268877, 2006.

(33) According to Hopf et al., phenolates can substitute both chlorines of dichloromethane, leading to di(aryloxy)methanes and chloride. Here, the reaction may occur according to $2AHX^- + CD_2Cl_2 \leftrightarrow CD_2A_2 + 2HX + 2Cl^-$, $AHX^- + HX \leftrightarrow AHX^-HX$, leading to higher accociates depending on concentrations and temperature. Hopf, H.; Utermoehlen, R.; Jones, P. G.; Desvergne, J. P.; Bouas-Laurent, H. *J. Org. Chem.* **1992**, *57*, 5509–5517.

(34) Siano, D. B.; Metzler, D. E. *J. Chem. Phys.* **1969**, *51*, 1856–1861.

(35) Chauvel, J. P., Jr.; True, N. S. *Chem. Phys.* **1985**, *95*, 435–441.

(36) Guillaume, F.; Séguin, J. P.; Nadio, L.; Uzan, R. *Spectrochim. Acta A* **1982**, *38*, 661–664.

(37) Steiner, T.; Majerz, I.; Wilson, C. C. *Angew. Chem., Int. Ed.* **2001**, *40*, 2651–2654.

(38) (a) Kiefer, P. M.; Hynes, J. T. *J. Phys. Chem. A* **2002**, *106*, 1834–1849. (b) Kiefer, P. M.; Hynes, J. T. *J. Phys. Chem. A* **2002**, *106*, 1850–1861. (c) Kiefer, P. M.; Hynes, J. T. *J. Phys. Chem. A* **2003**, *107*, 9022–9039.